

# StreakNet-Arch: An Anti-scattering Network-based Architecture for Underwater Carrier LiDAR-Radar Imaging

Xuelong Li, *Fellow, IEEE*, Hongjun An, Guangying Li, Xing Wang, Guanghua Cheng, and Zhe Sun

**Abstract**—In this paper, we introduce StreakNet-Arch, a novel signal processing architecture designed for Underwater Carrier LiDAR-Radar (UCLR) imaging systems, to address the limitations in scatter suppression and real-time imaging. StreakNet-Arch formulates the signal processing as a real-time, end-to-end binary classification task, enabling real-time image acquisition. To achieve this, we leverage Self-Attention networks and propose a novel Double Branch Cross Attention (DBC-Attention) mechanism that surpasses the performance of traditional methods. Furthermore, we present a method for embedding streak-tube camera images into attention networks, effectively acting as a learned bandpass filter. To facilitate further research, we contribute a publicly available streak-tube camera image dataset. The dataset contains 2,695,168 real-world underwater 3D point cloud data. These advancements significantly improve UCLR capabilities, enhancing its performance and applicability in underwater imaging tasks. The source code and dataset can be found at <https://github.com/BestAnHongjun/StreakNet>.

**Index Terms**—Underwater laser imaging, Signal processing, Streak-tube camera, LiDAR-Radar, Attention mechanism.

## I. INTRODUCTION

UNDERWATER laser imaging signal processing technology is crucial for obtaining underwater images, including 2D gray-scale maps and 3D point clouds images, which has wide applications in ocean exploration, biology [1], surveillance [2], archaeology, unmanned underwater vehicles control [3, 4], etc. In contrast to image processing algorithms for underwater image enhancement [5–13] or restoration [14–16], underwater laser imaging signal processing technology can process signals from a more fundamental source, such as streak-tube cameras and ICCD cameras. This approach enables the achievement of superior spatial resolution and extended detection ranges. However, its effectiveness is significantly hindered by a major challenge: scattering. This phenomenon drastically reduces image clarity and limits imaging range.

This research was supported by the China National Key R&D Program (2022YFC2808003), the Fundamental Research Funds for the Central Universities (D5000220481), and the Natural Science Foundation of Shaanxi Province, China (2024JC-YBMS-468).

Xuelong Li, Hongjun An, Guanghua Cheng and Zhe Sun are with School of Artificial Intelligence, Optics and ElectroNics (iOPEN), Northwestern Polytechnical University, Xi'an 710072, Shaanxi, China. Xuelong Li is also with the Institute of Artificial Intelligence (TeleAI), China Telecom Corp Ltd, Beijing 100033, China

Guangying Li and Xing Wang are with State Key Laboratory of Transient Optics and Photonics, Xi'an Institute of Optics and Precision Mechanics of CAS, Xi'an 710119, Shaanxi, China.

Corresponding author: Zhe Sun (sunzhe@nwpu.edu.cn).

To address this, the Underwater Carrier LiDAR-Radar (UCLR) employs a suite of strategies to suppress scattering and achieve long-distance underwater imaging [17–20]. Specifically, the UCLR's laser source typically utilizes blue or green light to minimize propagation attenuation in water [21], thereby enhancing detection distance. Additionally, a range-gated detector is employed for the UCLR, which is sensitive only to reflected signals received within a specific time window after the pulse is emitted. More importantly, lasers are modulated into high-frequency pulses to exceed the cut-off frequency of water's low-pass response [22, 23], effectively suppressing light scattering. Since the frequency is typically high ( $\geq 100$  MHz), receivers employing high temporal resolution optical detection devices are required, such as nanosecond-resolution ICCD cameras [24] or picosecond-resolution streak-tube cameras [25]. Underwater laser imaging relies on signal processing algorithms to extract target echoes from the received signal. These algorithms determine the presence and arrival time of the echoes, ultimately reconstructing the image. The processing typically involves two stages: scatter suppression and echo identification. Scatter suppression methods in the UCLR include bandpass filtering [25], adaptive filtering [26–31], and machine learning-based filtering [32]. The objective is to process a signal containing scatter noise into a suppressed scatter signal. Echo identification methods in UCLR primarily rely on thresholding techniques, including manually set thresholds [25] and adaptive thresholds [33], often coupled with matched filtering approaches [25]. These methods aim to determine the presence of echo signals in the received signal.

However, despite demonstrably mitigating scattering effects, these algorithms exhibit limitations in two key areas. Considering one aspect, low filtering accuracy leads to the loss of valuable information within the signal processing. Bandpass filtering algorithms rely on manually designed filters [25], where the bandpass range is determined empirically by engineers and may not necessarily be optimal. Alternatively, limitations in either algorithm complexity or real-time performance hinder their use for real-time underwater laser imaging. Adaptive filtering algorithms were primarily explored from the 1960s to the 1980s [26–31], and the existing machine learning filtering algorithms [32] mainly rely on traditional McCulloch-Pitts (MP) neural networks [34]. Constrained by the computational capabilities of hardware available at that time, these models have a limited number of parameters, resulting in a relatively low upper limit on performance.

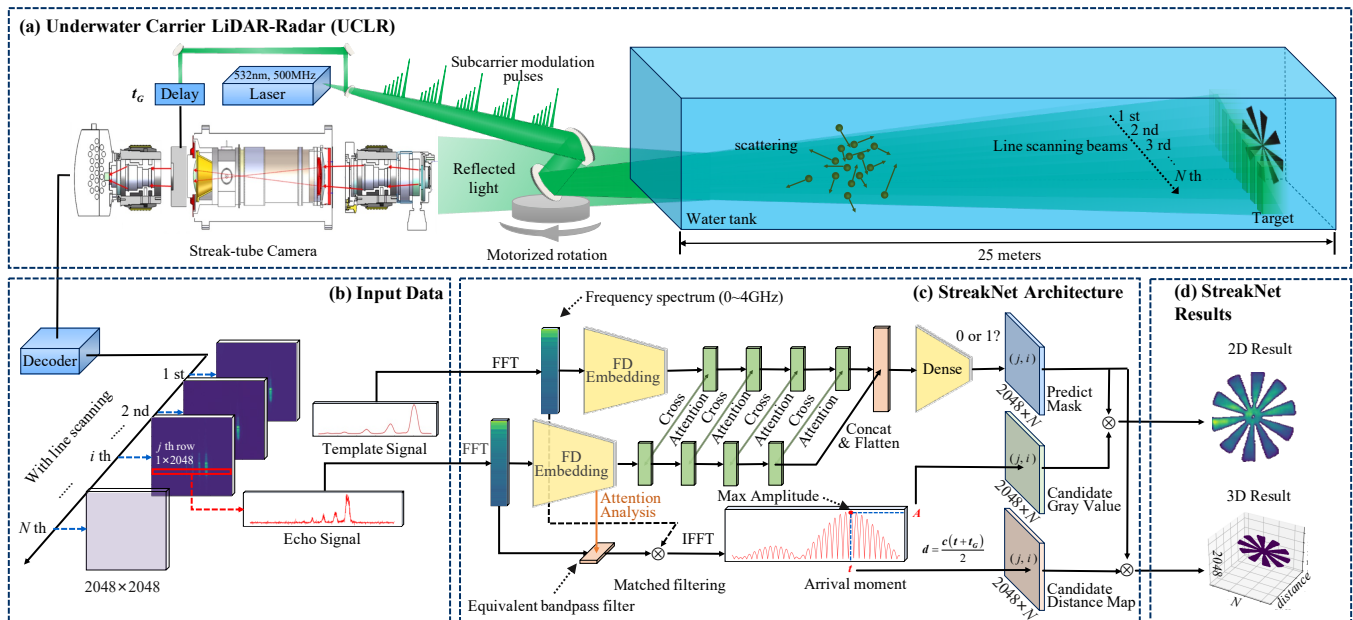


Fig. 1. Overview of the StreakNet-Arch based UCLR system.

Moreover, the current two-stage signal processing paradigm fails to achieve real-time imaging. This limitation arises from the echo identification in the second stage. Here, determining the threshold for identifying echoes requires denoising all collected scene signals and analyzing their statistical amplitude characteristics [25, 33]. This limitation severely constrains the practical utility of the UCLR.

In this paper, we experimented with employing Self-Attention mechanism networks [35] in the signal processing phase of the UCLR to improve the scatter resistance performance. This network architecture, achieving state-of-the-art (SOTA) performance in diverse fields like computer vision [36–40] and natural language processing [35, 41, 42], emerges as a powerful candidate for a universal model. To prevent network overfitting to the signal itself and enhance the network’s generalization ability across different scenes, we also provide a template signal alongside the input signal. This guides the network to discern the presence of echo signals by learning the differences between the signal and the template signal. To this end, we have made adjustments to the Self-Attention mechanism, introducing a Double Branch Cross Attention (DBC-Attention) mechanism, which our experiments have proven to be more suited for underwater imaging tasks. Furthermore, addressing the limitations of existing algorithms in real-time imaging, we depart from the conventional two-stage processing paradigm. Instead, we formulate the task as an end-to-end binary classification. This approach directly determines whether an input signal contains echoes, thereby equipping the UCLR with the capability for real-time imaging. Given that our scene dataset is acquired using a streak-tube camera, and the signals extracted from captured streak images serve as inputs for the network, we have named this end-to-end architecture StreakNet-Arch.

The main contributions of this paper can be summarized as

follows:

- 1) **StreakNet-Arch: Enabling Real-Time Imaging.** We introduce StreakNet-Arch, a novel end-to-end binary classification architecture that revolutionizes the UCLR’s signal processing. This approach empowers the UCLR with real-time imaging capabilities for the first time.
- 2) **DBC-Attention: Optimized for Underwater Environments.** We enhance the UCLR’s signal processing with Self-Attention networks. Further, we propose DBC-Attention, a groundbreaking variant specifically optimized for underwater imaging tasks. Experimental results conclusively demonstrate DBC-Attention’s superiority over the standard Self-Attention approach.
- 3) **Learned Bandpass Filtering with Streak-Tube Camera Integration.** We propose a method to embed streak-tube camera images directly into the attention network. This embedded representation effectively functions as a learned bandpass filter, as demonstrated by our experiments.
- 4) **Dataset.** We released a large-scale dataset containing 2,695,168 real-world underwater 3D point cloud data captured by streak-tube camera, which facilitates further development of Underwater laser imaging signal processing techniques.

## II. RELATED WORK

### A. Signal processing algorithms of UCLR

The signal processing algorithms for underwater laser imaging can be broadly categorized into two stages: scatter suppression and echo identification. Scatter suppression aims to process a signal containing scatter noise into a scatter-suppressed signal. Conventional methods primarily involve bandpass filtering [25], where engineers define a frequency bandpass range

based on their experiential knowledge to suppress clutter noise. However, this approach is limited by the subjective expertise of engineers and may not always yield optimal results. From the 1960s to the 1980s, researchers explored various adaptive filtering techniques to address limitations in bandpass filtering. These techniques, including lattice filters [26] and least squares lattice algorithms [27], operate in the time domain. Additionally, there were frequency domain methods such as the LMS algorithm [29] and its variants like FLMS [30] and UFLMS [31]. Subsequently, scholars combined machine learning algorithms based on MP neural networks to achieve adaptive clutter suppression [32].

In the UCLR, echo identification methods primarily rely on thresholding techniques. These encompass manually setting thresholds [25] and adaptive thresholding [33], often in conjunction with matched filtering methodologies [25], with the aim of identifying the presence of echo signals within the input signal.

### B. Attention Mechanism

In the past decade, the attention mechanism has played an increasingly important role in computer vision and natural language processing. In 2014, Mnih V. et al. [43] pioneered the use of attention mechanism into neural networks, predicting crucial regions through policy gradient recursion and updating the entire network end-to-end. Later, various works [44, 45] adopted a similar strategy for attention in vision, with recurrent neural networks (RNNs) serving as necessary tools. Hu J. et al. proposed SENet [36], presenting a novel channel-attention network that implicitly and adaptively predicts potential key features.

A significant shift came in 2017 with the introduction of the Self-Attention mechanism by Vaswani et al [35]. This advancement revolutionized Natural Language Processing (NLP) [41, 42]. In 2018, Wang et al. [37] took the lead in introducing Self-Attention to computer vision. Notably, Hu et al. (2018) also proposed a novel channel-attention network (SENet) within this timeframe. Recently, various deep Self-Attention networks (Visual Transformers, ViTs) [38–40, 46, 47] have appeared, showcasing the immense potential of attention-based models.

Attention mechanisms can also be applied to the enhancement of underwater image processing [5, 48, 49]. In 2023, Peng L. et al. introduced the U-shape Transformer, pioneering the incorporation of self-attention mechanisms into underwater image enhancement [5]. They proposed a Transformer module that fuses multi-scale features across channels, and a spatial module for global feature modeling. This innovation enhances the network’s focus on areas of more severe attenuation in both color channels and spatial regions. Mehnaz U. et al. proposed an innovative Underwater window-based Transformer Generative Adversarial Network (UwTGAN) aimed at enhancing underwater image quality for computer vision applications in marine settings [48]. Pramanick A. et al. propose a framework called X-CAUNET that considered wavelength of light in underwater conditions by using cross-attention transformers [49].

## III. METHOD

### A. StreakNet-Arch

The proposed StreakNet-Arch based UCLR system (Fig. 1a-d) employs a sub-nanosecond Q-switch laser to generate subcarrier-modulated pulses at a frequency of 500 MHz with 532 nm. A portion of the generated pulse passes through the beam splitter into a delay device, which can be gated by a delay of  $t_G$  seconds.<sup>1</sup> After the delay, a trigger signal is sent to the control circuit of the streak-tube camera. Simultaneously, another part of the pulse is reflected into the water tank.

By rotating the motorized turntable, a line scan of remote underwater objects is achieved. The reflected light from the objects reaches the streak-tube camera. Upon decoding, a series of streak-tube images is generated (Fig. 1b).

For the line scan containing  $N$  discrete angles, the system will generate  $N$  streak-tube images, each with dimensions of  $2048 \times 2048$ . The horizontal axis corresponds to the full-screen scanning time at that angle, while the vertical axis corresponds to space. For the  $j$ -th row of the  $i$ -th image, it represents the  $j$ -th ( $0 \leq j < 2048$ ) vertical spatial position for the  $i$ -th scanning angle ( $0 \leq i < N$ ), with the light intensity variation over 30ns time sampled as a  $1 \times 2048$  vector.

After inputting this vector along with a corresponding template signal vector into the StreakNet-Arch based UCLR system, the resulting output will correspond to the  $(j, i)$  component of both a 2D grayscale map and a 3D depth map, where the dimensions of both maps are  $2048 \times N$  (Fig. 1d).

### B. FD Embedding Layer

In section III-A, we introduce that the StreakNet-Arch’s inputs consist of an echo timing signal vector  $\mathbf{v}_{echo} \in \mathbb{R}^{1 \times N_s}$  and a template timing signal vector  $\mathbf{v}_{tem} \in \mathbb{R}^{1 \times L_{tem}}$  ( $L_{tem} \leq N_s$ ), where  $N_s = 2048$  in our project. With a full-screen scan time of  $T_{full} = 30$  ns and  $N_s$  samples taken, the signal vector is sampled at a frequency of 68.27 GHz (see Eq. 1).

$$f_s = \frac{N_s}{T_{full}}. \quad (1)$$

The two vectors will be firstly fed into the Frequency Domain (FD) Embedding Layer (FDEL) of the network. Upon entering the FDEL, the vectors will undergo a Fast Fourier Transform (FFT). During the transformation, the lengths of the two vectors will be standardized by padding with zeros up to  $N_{FFT}$ , to obtain an appropriate frequency resolution  $\Delta R_f$  after the transformation. In our work, we set  $N_{FFT}$  to be  $2^{16}$ , hence the frequency resolution is approximately 1 MHz. (see Eq. 2).

$$\Delta R_f = \frac{f_s}{N_{FFT}}. \quad (2)$$

After the transformation, a spectrum of length  $N_{FFT}$  will be obtained, corresponding to a frequency range of 0 to  $f_s/2$ . However, the carrier frequency  $f_c$  is typically much smaller

<sup>1</sup>Range-gated imaging technology, which captures images by controlling the camera shutter delay for a certain period  $t_G$ . This enables the reception of signals within a specific range, mitigating the impact of backscattering on imaging.

than  $f_s/2$ , so only the portion of the frequency vector from index 0 to  $L = k\lceil f_c/\Delta R_f \rceil$  is usually retained, where  $k$  is a correction factor. (see Eq. 3). In our work, we set  $L$  to be 4000, meaning only frequency components up to approximately 4 GHz are retained.

$$\begin{aligned} \mathbf{u}_{\text{echo}} &= \mathcal{F}\mathcal{F}\mathcal{T}(\mathbf{v}_{\text{echo}}, N_{\text{FFT}})[0:L], \\ \mathbf{u}_{\text{tem}} &= \mathcal{F}\mathcal{F}\mathcal{T}(\mathbf{v}_{\text{tem}}, N_{\text{FFT}})[0:L]. \end{aligned} \quad (3)$$

It is worth noting that from an engineering point of view, the current neural network under the PyTorch framework [50] does not support vector inputs of imaginary numbers. So we introduce an imaginary expansion operator (IEO) (see Eq. 4) to convert the imaginary vector ( $\mathbf{u} \in \mathbb{C}^{1 \times L}$ ) to a real vector ( $\mathbf{u}' \in \mathbb{R}^{1 \times 2L}$ ).

$$\text{IEO}:\mathbf{u}'_k = \begin{cases} \text{Re}(\mathbf{u}_k), & 0 \leq k < L, \\ \text{Im}(\mathbf{u}_{k-L}), & L \leq k < 2L. \end{cases} \quad (4)$$

$$\begin{aligned} \mathbf{u}'_{\text{echo}} &= \text{IEO}(\mathbf{u}_{\text{echo}}), \\ \mathbf{u}'_{\text{tem}} &= \text{IEO}(\mathbf{u}_{\text{tem}}). \end{aligned} \quad (5)$$

After applying IEO (see Eq. 5), two vectors of length  $2L$  are obtained. Clearly, not every component significantly contributes to the recognition task. Therefore, a linear layer (see Eq. 6) is subsequently applied for feature extraction. Now introducing a width factor, denoted as  $\lambda_w$  ( $0 \leq \lambda_w \leq 1$ , with official recommendations of 0.125, 0.25, 0.50, or 1.00), the input dimension of the linear layer is set to  $2L$ , and the output dimension is  $\lfloor 512\lambda_w \rfloor$ .

$$\begin{aligned} \mathbf{X}_{\text{echo}}^{\top} &= \text{SiLU}(\mathbf{W}_{\text{echo}}\mathbf{u}'_{\text{echo}} + b_{\text{echo}}), \\ \mathbf{X}_{\text{tem}}^{\top} &= \text{SiLU}(\mathbf{W}_{\text{tem}}\mathbf{u}'_{\text{tem}} + b_{\text{tem}}), \end{aligned} \quad (6)$$

where  $\mathbf{W}_* \in \mathbb{R}^{\lfloor 512\lambda_w \rfloor \times 2L}$  and  $b_* \in \mathbb{R}$  are respectively the learnable weight matrix and bias. The  $\mathbf{X}_* \in \mathbb{R}^{1 \times \lfloor 512\lambda_w \rfloor}$  are outputs of the FDEL.

### C. Attention Analysis Method

We leverage attention analysis to elucidate the learning mechanism of the FDEL. Our experiments demonstrate that the FDEL effectively functions as a learned bandpass filter.

From the perspective of MP neuron model [34], the linear layer is essentially a series of input nodes and MP neurons, and the weight matrix is the connection weight between input nodes and neurons. If we want to calculate the input of  $j$ -th neuron, we need to multiply all the input nodes by their respective weights and then sum them (see Eq. 7).

$$y_j = \sum_{i=0}^{N_{\text{input}}} w_{ij} \cdot x_i. \quad (7)$$

This perspective is from the viewpoint of neurons (Fig. 2a). If we reverse the view to consider it from the perspective of input nodes (Fig. 2b), for input node  $i$ , if there is a connection weight  $w_{ij}$  with neuron  $j$ , it implies that neuron  $j$  has extracted the quantity of information  $\|w_{ij}\|$  from node  $i$ . In other words,

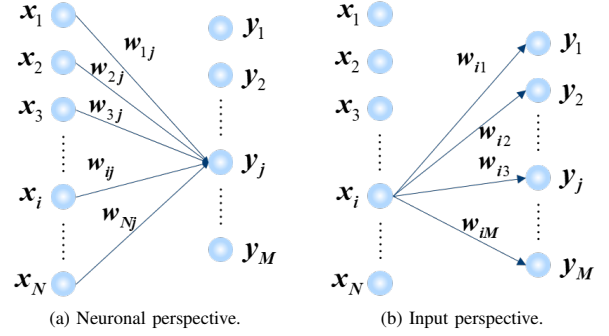


Fig. 2. Different perspectives of MP model.

neuron  $j$  has allocated its attention to node  $i$  through the weight  $\|w_{ij}\|$ . If neuron  $j$  is completely indifferent to the information from node  $i$ , then  $w_{ij}$  should be equal to 0. In that case, the total attention of the neural network to input node  $i$  should be expressed by Eq. 8.

$$A'_i = \sum_{j=0}^{N_{\text{neurons}}} \|w_{ij}\|. \quad (8)$$

Standardize the attention to unify units (see Eq. 9). The above process can be called Attention Analysis Method (AAM). If we perform an Attention Analysis on the weight matrix  $\mathbf{W}_{\text{echo}}$  of the FDEL, the resulting attention distribution can be equivalent to the transfer function of a bandpass filter.

$$\begin{aligned} A_i &= \frac{A'_i - \min\{A'_i\}}{\max\{A'_i\} - \min\{A'_i\}}, \\ \mathbf{A} &= (A_i)_{1 \times 2L}, \end{aligned} \quad (9)$$

where  $\mathbf{A}$  is the filtering transfer function.

### D. Double Branch Cross Attention Backbone

Double Branch Cross Attention (DBC-Attention) is a special attention mechanism. For the input of two branches  $\mathbf{X}_{\text{echo}}, \mathbf{X}_{\text{tem}} \in \mathbb{R}^{1 \times \lfloor 512\lambda_w \rfloor}$ , they are alternatively utilized as keys, values, and queries to compute the attention scores. Subsequently, upon aggregating the attention, the double branch deep feature tensors  $\mathbf{Y}_{\text{echo}}, \mathbf{Y}_{\text{tem}} \in \mathbb{R}^{1 \times \lfloor 512\lambda_w \rfloor}$  are generated through a nonlinear feedforward network.

The formal representation is as follows: Firstly, the keys, values, and queries are computed (see Eq. 10).

$$\begin{aligned} \mathbf{Q}_1 &= \mathbf{W}_{q1}\mathbf{X}_{\text{echo}}, \mathbf{Q}_2 = \mathbf{W}_{q2}\mathbf{X}_{\text{tem}}, \\ \mathbf{K}_1 &= \mathbf{W}_{k1}\mathbf{X}_{\text{tem}}, \mathbf{K}_2 = \mathbf{W}_{k2}\mathbf{X}_{\text{echo}}, \\ \mathbf{V}_1 &= \mathbf{W}_{v1}\mathbf{X}_{\text{tem}}, \mathbf{V}_2 = \mathbf{W}_{v2}\mathbf{X}_{\text{echo}}, \end{aligned} \quad (10)$$

where  $\mathbf{W}_*$  are learnable parameters. Then, attention scores are computed and attention is aggregated. The residual method is employed by adding it to the input and followed by Layer Normalization (LNORM) [51] (see Eq. 11):



$$\begin{aligned} \mathbf{Y}_1 &= \text{LNorm} \left[ \mathbf{X}_{\text{echo}} + \text{softmax} \left( \frac{\mathbf{Q}_1 \mathbf{K}_1^\top}{\sqrt{d_k}} \right) \mathbf{V}_1 \right], \\ \mathbf{Y}_2 &= \text{LNorm} \left[ \mathbf{X}_{\text{tem}} + \text{softmax} \left( \frac{\mathbf{Q}_2 \mathbf{K}_2^\top}{\sqrt{d_k}} \right) \mathbf{V}_2 \right], \end{aligned} \quad (11)$$

where  $d_k$  is the column space dimension of the input/output tensor. Finally, the deep feature tensor is output through the feedforward layer. The residual method is also used here (see Eq. 12).

$$\begin{aligned} \mathbf{Y}_{\text{echo}} &= \text{SiLU} \left[ \text{LNorm} (\mathbf{W}_1 \mathbf{Y}_1^\top + \mathbf{Y}_1^\top + b_1) \right], \\ \mathbf{Y}_{\text{tem}} &= \text{SiLU} \left[ \text{LNorm} (\mathbf{W}_2 \mathbf{Y}_2^\top + \mathbf{Y}_2^\top + b_2) \right], \end{aligned} \quad (12)$$

where  $\mathbf{W}_*$  and  $b_*$  are learnable parameters, and SiLU [52] is a type of nonlinear activation function.

Eq. 10-12 together form the basic block of DBC-Attention. Similar to the Transformer architecture [35], DBC-Attention can use a multi-head attention approach when calculating scores.

By stacking different numbers of DBC-Attention blocks, we can obtain backbone networks with different depths for DBC-Attention architecture.

### E. Imaging Head

The Imaging Head consists of two main data paths: the denoising path and the imaging path. The denoising path is used to determine whether the feature tensor of the input echo signal of the network contains a target, producing a mask map. This aims to replace the handcraft threshold used in traditional algorithms and can be modeled as a binary classification task. The imaging path builds upon traditional imaging methods but incorporates an equivalent filter learned through AAM during the filtering process. This learned filter replaces traditional handcrafted bandpass filters, resulting in candidate gray and distance maps. Finally, the mask map from the denoising path is multiplied element-wise with the gray and distance maps generated by the imaging path to produce the final imaging outputs.

#### • Denoising path:

The output  $\mathbf{Y}_{\text{echo}}, \mathbf{Y}_{\text{tem}}$  from backbone network is concatenated, and then passed through a feedforward layer to obtain a binary probability vector  $\mathbf{Y}$  (see Eq. 13).

$$\begin{aligned} \mathbf{Y}' &= \text{Concat} (\mathbf{Y}_{\text{echo}}, \mathbf{Y}_{\text{tem}}), \\ \mathbf{Y}^\top &= \text{SiLU} (\mathbf{W} \mathbf{Y}'^\top + b), \end{aligned} \quad (13)$$

where  $\mathbf{W}$  and  $b$  are learnable parameters. The mask map  $\mathbf{M}$  is calculated using Eq. 14:

$$\mathbf{M}(j, i) = \text{argmax}(\mathbf{Y}). \quad (14)$$

#### • Imaging path:

First, the vector obtained from Eq. 4 is multiplied by the transfer function obtained through the AAM method (Eq. 9) to perform filtering operations (see Eq. 15).

$$\boldsymbol{\mu}'_{\text{echo}} = \mathbf{u}'_{\text{echo}} \odot \mathbf{A}. \quad (15)$$

Next, the Inverse Imaginary Expansion Operator (IIEO) (Eq. 16) is used to transform the real vector  $\boldsymbol{\mu}'_{\text{echo}} \in \mathbb{R}^{1 \times 2L}$  into a complex vector  $\boldsymbol{\mu}_{\text{echo}} \in \mathbb{C}^{1 \times L}$  (see Eq. 17).

$$\text{IIEO}(\boldsymbol{\mu}'): \boldsymbol{\mu}_k = \boldsymbol{\mu}'_k + i \boldsymbol{\mu}'_{k+L}. \quad (16)$$

$$\boldsymbol{\mu}_{\text{echo}} = \text{IIEO}(\boldsymbol{\mu}'_{\text{echo}}). \quad (17)$$

Then, multiply  $\boldsymbol{\mu}_{\text{echo}}$  by the spectrum of template signal  $\mathbf{u}_{\text{tem}}$ , perform frequency-domain matched filtering (Eq. 18), and transform back to the time domain using inverse fast Fourier transform (Eq. 19).

$$\boldsymbol{\psi} = \boldsymbol{\mu}_{\text{echo}} \odot \mathbf{u}_{\text{tem}}. \quad (18)$$

$$\mathbf{v}_f = \mathcal{IFFT}(\boldsymbol{\psi}, N_{\text{FFT}})[0 : N_s], \quad (19)$$

where  $\mathbf{v}_f \in \mathbb{R}^{1 \times N_s}$  time domain signal of scattering suppression. The candidate gray map ( $\mathbf{CG}$ ) and candidate distance map ( $\mathbf{CD}$ ) can be calculated as follows (Eq. 20):

$$\begin{aligned} i &= \text{argmax}(\mathbf{v}_f), \\ t &= i \frac{1}{f_s} + t_G, \\ \mathbf{CG}(j, i) &= \max(\mathbf{v}_f), \\ \mathbf{CD}(j, i) &= \frac{c}{n} \cdot \frac{t}{2}, \end{aligned} \quad (20)$$

where  $f_s$  is the sample frequency (Eq. 1),  $t_G$  is the gate time,  $c$  the speed of light in vacuum, and  $n$  is the refractive index of the propagation medium.

#### • Path aggregation:

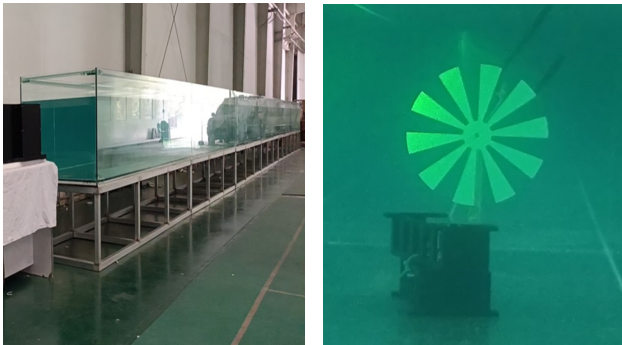
By multiplying with the mask map  $\mathbf{M}$ , we obtain the gray map  $\mathbf{G}$  and distance map  $\mathbf{D}$  (see Eq. 21).

$$\begin{aligned} \mathbf{G} &= \mathbf{CG} \odot \mathbf{M}, \\ \mathbf{D} &= \mathbf{CD} \odot \mathbf{M}. \end{aligned} \quad (21)$$

### F. Loss Function

The loss function is the objective optimization function during the training phase. It is worth noting that although the Imaging Head contains a denoising path and imaging path, only the denoising path participates in the training process. The echo signal vector  $\mathbf{v}_{\text{echo}}$  and the template signal vector  $\mathbf{v}_{\text{tem}}$  sequentially pass through FD Embedding Layer, backbone network, and the denoising path of the Imaging Head to obtain a binary probability vector  $\mathbf{Y}$ , which represents the complete forward propagation process. Since this task can be modeled as a binary classification task, we choose cross-entropy as the loss function (Eq. 22).

$$\mathcal{L}(\mathbf{Y}, \mathbf{Y}') = - \sum_{i=0}^2 Y'_i \log(Y_i). \quad (22)$$



(a) 25 m experimental water tank. (b) 30 cm diameter experimental target.

Fig. 3. Experimental setup.

### G. Datasets

The dataset was collected in a controlled environment, a 25 m long water tank (Fig. 3a). A target with a diameter of 30 cm (Fig. 3b) was positioned at varying distances (10 m, 13 m, 15 m, and 20 m) within the tank, and data was collected using the UCLR system.  $N_d$  discrete angles were captured at each distance, and the resolution of the streak-tube images was  $2048 \times 2048$ . Since each row vector of the image serves as the input unit for the algorithm, each image can provide 2048 samples.  $N_d$  images captured at distance  $d$  generate a total of  $2048 \cdot N_d$  samples, for example, we collected  $N_{20m} = 267$  images at the distance of 20 m, then we could have  $2048 \times 267 = 546,816$  samples. These  $2048 \times 267$  samples were manually annotated into a  $2048 \times 267$  binary map, with each pixel assigned a value of either 0 or 1. Here, a pixel value of 0 indicates that the corresponding sample signal comprises background noise, whereas a value of 1 signifies that the sample signal contains target echoes.

Subsequently, the samples were manually divided into different subsets: approximately 40% were allocated to the training set, which is highlighted in red in Fig. 4a. This subset was used for network training. About 5% of the samples were designated as the validation set, utilized for periodic evaluation of network performance during training to ensure that the best checkpoint was saved. This validation set was also utilized for performance comparison between StreakNets, StreakNets-Emb, and traditional imaging methods, as highlighted in Fig. 4b. Using only 5% for validation was intended to expedite the training process. This validation subset was carefully selected to include noise and target samples that were isolated from the training dataset, ensuring representativeness. To ensure comprehensive visualization, all data samples (100%) were designated for a final test set. This set served solely for the creation of the final image visualizations depicted in the red area of Fig. 4c and was explicitly excluded from the performance evaluation metrics.

The partitioning method at other distances was similar to that at 20 m. In total, our dataset included 2,695,168 samples. Table I provides a breakdown of the number of images captured at each distance, the aggregate number of samples, and their allocation into the training and validation datasets.

TABLE I  
DETAILS OF THE DATASET.

$d$	Resolution	$N_d$	Test set	Training set	Validation set
10 m	$2048 \times 2048$	400	819,200	315,200	40,800
13 m	$2048 \times 2048$	349	714,752	281,992	47,530
15 m	$2048 \times 2048$	300	614,400	245,400	39,200
20 m	$2048 \times 2048$	267	546,816	229,086	31,240
Total	$2048 \times 2048$	1316	2,695,168	1,071,678	158,770

## IV. EXPERIMENTS

### A. Model training

Under the StreakNet-Arch, we simultaneously trained StreakNet with the Self-Attention mechanism as the backbone network and StreakNetv2 with the DWC-Attention mechanism for comparative experiments.

During the training phase, the Stochastic Gradient Descent (SGD) algorithm is used to optimize for 120 epochs, with a base learning rate of  $2 \times 10^{-6}$  per batch. A cosine annealing learning rate strategy is employed (Fig. 5), and the Exponential Moving Average (EMA) method is used. The training was performed on a single NVIDIA RTX 3090 (24G). The parameters of all trained models are shown in Table II. After training, the loss decreased by approximately 70% (Fig. 6).

TABLE II  
THE PARAMETERS OF MODEL TRAINING.

Model name	Backbone architecture	$\lambda_w$	Number of layers	Number of heads
StreakNet-s	Self-Attention	0.125	1	2
StreakNet-m	Self-Attention	0.250	2	4
StreakNet-l	Self-Attention	0.500	4	8
StreakNet-x	Self-Attention	1.000	8	16
StreakNetv2-s	DBC-Attention	0.125	1	2
StreakNetv2-m	DBC-Attention	0.250	2	4
StreakNetv2-l	DBC-Attention	0.500	4	8
StreakNetv2-x	DBC-Attention	1.000	8	16

### B. StreakNet-Arch exhibits superior anti-scattering capabilities compared to traditional imaging methods

To address the challenge of anti-scattering, we formulate it as a binary classification task. This approach allows us to distinguish between pure noise and signal inputs containing target echoes. The  $F_1$  score, a well-established metric in classification tasks, is then employed to evaluate the model's anti-scattering effectiveness.

We will evaluate the 0-1 masks  $\hat{M}$  obtained from the StreakNets and the traditional imaging algorithms (see Fig. 1c,1f) using the labels provided by the dataset as ground truth  $M$ . The  $F_1$  score is calculated as Eq. 23.

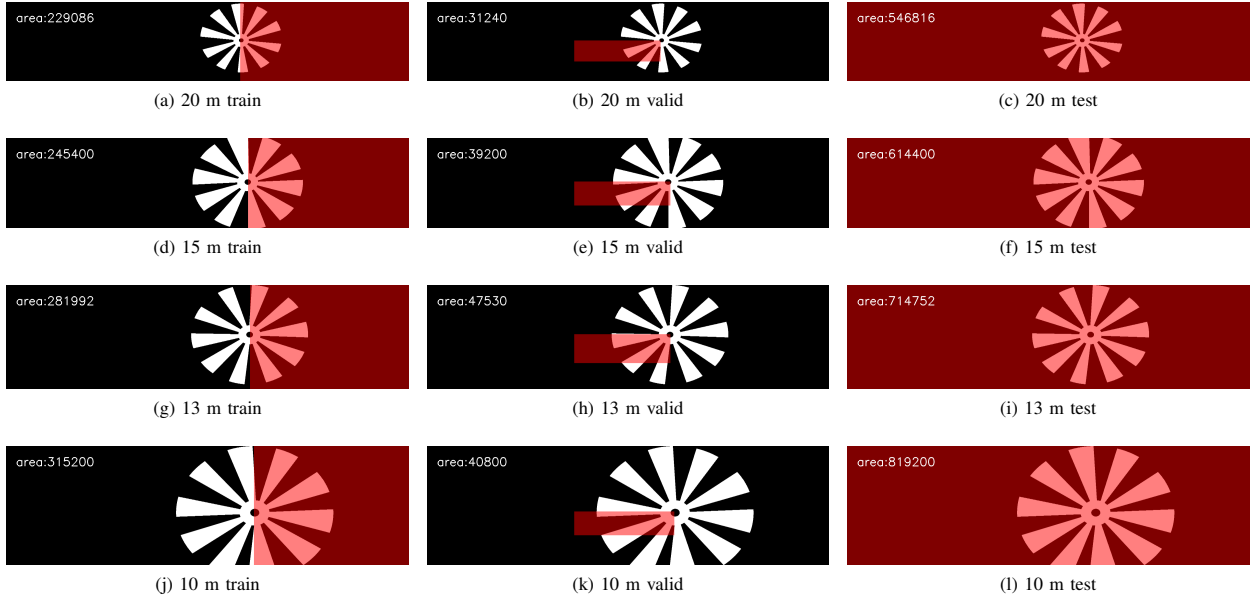


Fig. 4. Schematic diagram of dataset partitioning.

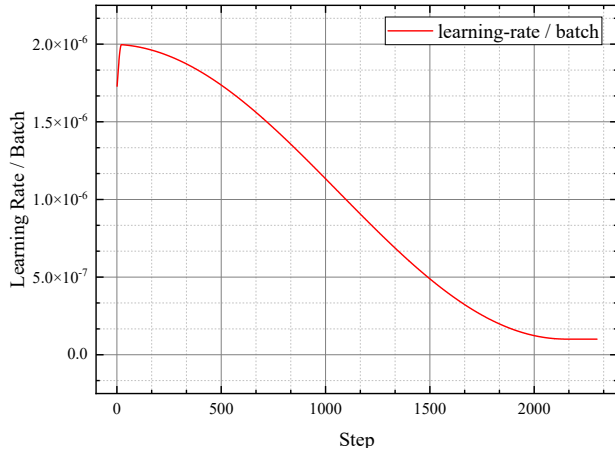


Fig. 5. Learning rate variation curve during the training phase.

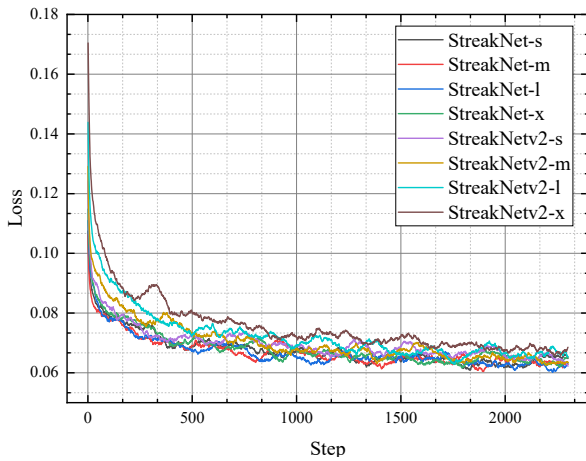
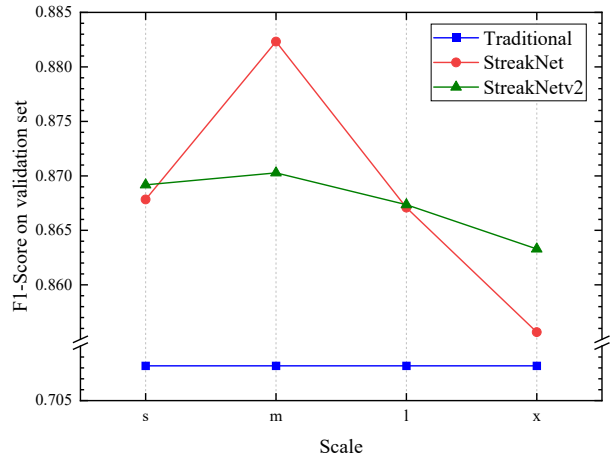


Fig. 6. Loss variation curve during the training phase.

$$\begin{aligned}
 TP &= \sum_i \sum_j \hat{M}_{ij} \wedge M_{ij}, \\
 FP &= \sum_i \sum_j \hat{M}_{ij} \wedge \neg M_{ij}, \\
 FN &= \sum_i \sum_j \neg \hat{M}_{ij} \wedge M_{ij}, \\
 P &= \frac{TP}{TP + FP}, \\
 R &= \frac{TP}{TP + FN}, \\
 F_1 &= \frac{2 \cdot P \cdot R}{P + R}.
 \end{aligned} \tag{23}$$

Fig. 7.  $F_1$  scores evaluated on the validation set for traditional algorithms and StreakNet.

We evaluated the traditional algorithms and the StreakNets on the validation set, and the results are shown in Fig. 7 and Table III. Clearly, both Self-Attention-based StreakNet

and DWC-Attention-based StreakNetv2 achieve higher  $F_1$  scores than traditional algorithms. This demonstrates that the StreakNet-Arch has stronger anti-scattering capabilities compared to traditional algorithms. The imaging results are shown in Fig. 8 and 9.

TABLE III  
 $F_1$  SCORES (%) FOR TRADITIONAL IMAGING METHODS AND STREAKNET-ARCH IMAGING METHODS ON THE VALIDATION SET.

Model	Traditional (baseline)	StreakNet		StreakNetv2	
s	70.82	86.78	+15.96	86.92	+16.10
m	70.82	88.23	<b>+17.41</b>	87.03	<b>+16.21</b>
l	70.82	86.71	+15.89	86.35	+15.92
x	70.82	85.57	+14.75	86.33	+15.51

### C. StreakNet-Arch is more suitable for real-time imaging than Traditional Imaging Methods

Traditional imaging algorithms require the integration of global grayscale information to determine the denoising threshold. Therefore, for each captured streak-tube image  $i(1 \leq i \leq N)$ , after processing for time  $t_{i1}$ , there is an additional pending time  $t_{i2}$  until all  $N$  streak-tube images are processed. Then, additional time  $t_0 \approx 0$  ( $t_0 \ll t_{i1}, t_{i2}$ ) is required to determine the threshold and complete the imaging process. Until the last streak-tube image is processed, we cannot obtain any imaging results (Fig. 10).

$$\begin{aligned}
 \text{AIT}_{\text{traditional}} &= \frac{1}{N} \sum_{i=1}^N t_{i1} + t_{i2} \\
 &= \frac{1}{N} \sum_{i=1}^N i t_{i1} \\
 &= \frac{N+1}{2} t_m.
 \end{aligned} \tag{24}$$

To measure the real-time imaging capability of the algorithm, we propose an evaluation metric called the Average Imaging Time (AIT), defined as the average time from the input of a streak-tube image to obtaining the corresponding imaging result. If we assume  $t_{11} = t_{21} = \dots = t_{N1} = t_m$ , the AIT for traditional imaging algorithms is calculated using Eq. 24.

However, for the StreakNet-Arch method, there is no need for global information to determine whether the current input signal contains target echoes. Therefore, compared to traditional imaging algorithms, the StreakNet-Arch method has no pending time. Instead, for the current input streak-tube image, it can directly generate the corresponding imaging result, as shown in Fig. 11. Its AIT can be calculated using Eq. 25.

$$\begin{aligned}
 \text{AIT}_{\text{streaknet}} &= \frac{1}{N} \sum_{i=1}^N t_{i1} \\
 &= t_m.
 \end{aligned} \tag{25}$$

It is evident that the AIT of the traditional imaging algorithm is a linear function with respect to  $N$ , while the AIT of StreakNet-Arch is a constant. Therefore, theoretically, in practical scenarios where  $N$  is large, StreakNet-Arch will have a significant advantage in real-time imaging. To validate this theory, we conducted a comparative experiment. We sequentially input  $N$  streak-tube images, where  $N$  gradually increases from 1 to 64, and tested the AIT metric for both traditional algorithms and StreakNet-Arch on an NVIDIA RTX 3060 (12G) GPU. Experimental results are depicted in Fig. 12 and Table IV, with AIT values measured in milliseconds (ms). The experimental findings indicate that as the number of streak-tube images increases from 2 to 64, the AIT for traditional imaging methods escalates linearly from 58 ms to 1257 ms. In contrast, the AIT for the StreakNet method remains constant within the range of 54 ms to 84 ms.

TABLE IV  
AIT (MS) FOR TRADITIONAL IMAGING ALGORITHMS AND STREAKNET-ARCH ALGORITHMS.

$N$	2	4	8	16	32	64
Traditional	58.05	96.72	174.1	328.8	638.2	1257
StreakNet-s	54.05	54.01	54.01	54.00	54.00	53.99
StreakNet-m	54.89	54.90	54.92	54.92	54.93	54.93
StreakNet-l	60.65	60.67	60.67	60.67	60.70	60.70
StreakNet-x	84.26	84.28	84.33	84.30	84.32	84.33
StreakNetv2-s	54.10	54.08	54.09	54.08	54.08	54.09
StreakNetv2-m	55.03	55.05	55.07	55.08	55.09	55.09
StreakNetv2-l	60.99	61.00	61.02	61.02	61.03	61.03
StreakNetv2-x	84.11	84.03	84.03	84.04	84.08	84.11

The experimental results validate the correctness of the theory: the AIT of the traditional imaging algorithm varies linearly with the number of images (the vertical axis is in logarithmic form in Fig. 12), while the AIT of StreakNet-Arch is a constant. When  $N > 4$ , the AIT of StreakNet-Arch is significantly better than that of the traditional algorithm, confirming that StreakNet-Arch is more suitable for real-time imaging tasks.

### D. FD Embedding Layer is an equivalent bandpass filter

To further explore the potential learning mechanisms of StreakNets, we performed AAM on the FD Embedding Layer of StreakNet-m and StreakNetv2-m, which performed best on the validation set, and visualized the attention distribution, as shown in Fig. 13.

Since the carrier frequency of the detection signal is 500 MHz (see Fig. 1e), traditional imaging algorithms use a handcraft bandpass filter with a range of 450 MHz - 550 MHz during filtering. If we consider the bandpass filter from the perspective of ‘‘attention distribution’’, we can think of the bandpass filter as a binary attention distribution with values of 1 for frequencies in the range of 450 MHz - 550 MHz and 0 for frequencies outside this range. Similarly, the attention distribution of the FD Embedding Layer can also be regarded as a generalized bandpass filter.



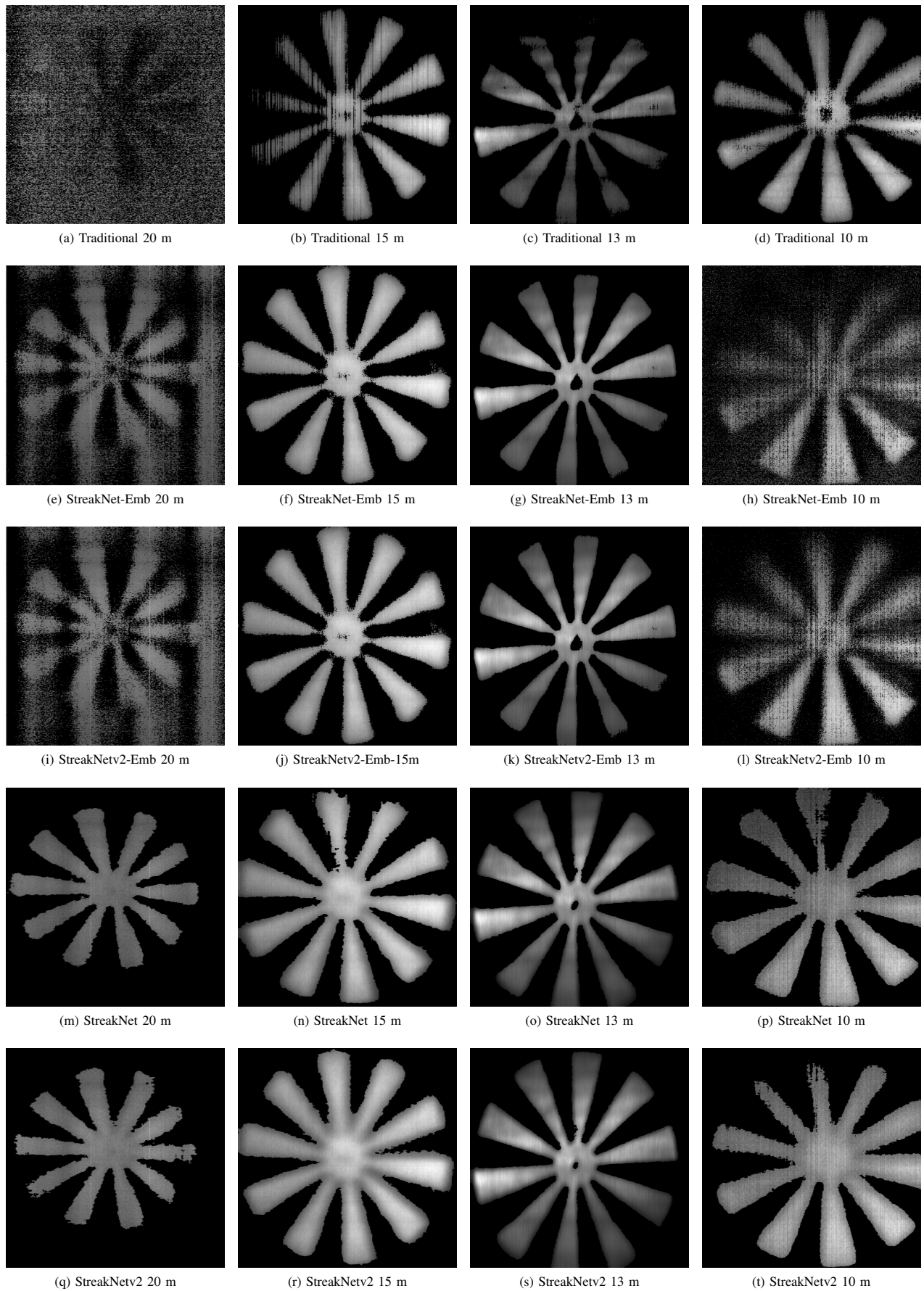


Fig. 8. 2D imaging experimental results under various distances for each method.



Fig. 9. 3D imaging experimental results under various distances for each method.

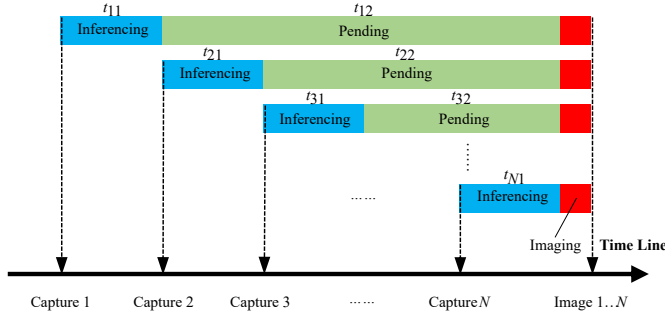


Fig. 10. The sequence chart of traditional imaging algorithm.

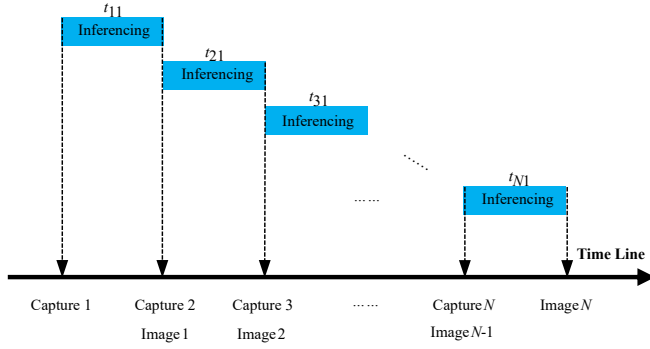


Fig. 11. The sequence chart of StreakNet-Arch method.

In Fig. 13a and Fig. 13b, we observed that the FD Embedding Layer has a significant attention towards frequencies near 500 MHz, which closely matches the range of the traditional bandpass filtering algorithm within an acceptable margin of error. However, apart from frequencies near 500 MHz, the highest attention appears around 40 MHz, which seems counterintuitive.

Therefore, we further enumerated the range of bandpass filters in the range of 0 - 200 MHz, with each group spanning 5 MHz, and used traditional methods for imaging. We then calculated the  $F_1$  score on the validation set. The experimental

results are shown as the red curve in Fig. 14a. A peak appears at 42.5 MHz (i.e., the 40 MHz - 45 MHz bandpass range), indicating that frequency information near 40 MHz is indeed strongly correlated with anti-scattering imaging.

After consulting the literature on physical optics, we found that Perez et al. proposed a physical model for the frequency response of water in 2012 [53], called  $\mathcal{M}$  Function, as shown in Eq. 26.

$$\mathcal{M}(\Delta Z) = \sqrt{1 + e^{-2\varepsilon\Delta Z} - 2e^{-\varepsilon\Delta Z} \cos(K\Delta Z)}, \quad (26)$$

where  $\mathcal{M}$  represents the ratio of the amplitude of the output signal frequency component to that of the input signal, i.e., the transfer function.  $\varepsilon$  is the attenuation coefficient,  $\Delta Z$  is half the wavelength corresponding to the carrier frequency, and  $K$  is the number of carrier pulses.

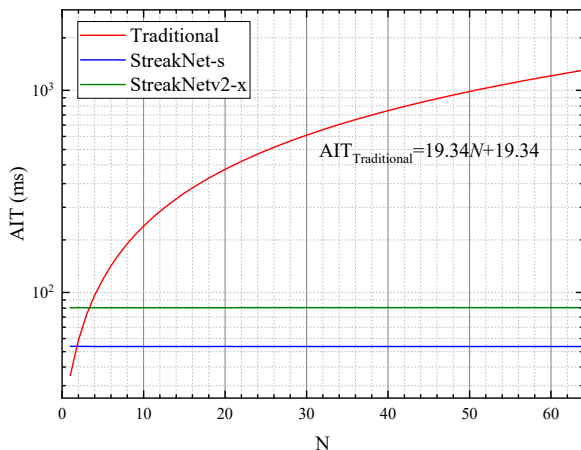
In our experiment, the attenuation coefficient  $\varepsilon$  of water is 0.11, and the number of carrier pulses  $K$  is 4. The  $\mathcal{M}$  Function curve plotted is shown as the blue curve in Fig. 14a. And surprisingly, it is found that within an acceptable error range, there is indeed a peak near 40 MHz. By plotting the  $\mathcal{M}$  Function and the attention distribution of the FD Embedding Layer on the same Fig. 15, it is also found that this peak almost perfectly overlaps.

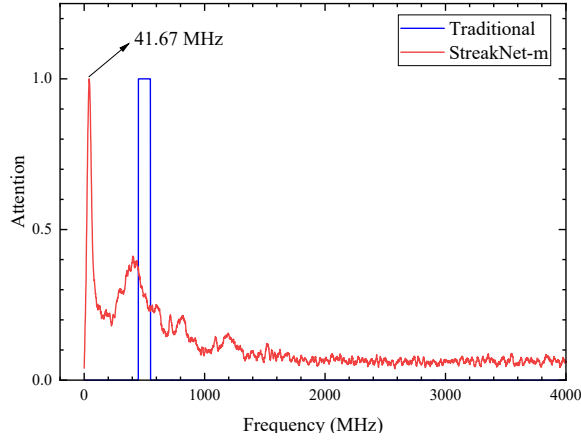
The experiments above indicate that StreakNets have learned from a large amount of sample data and discovered that frequency components near 40 MHz have a greater impact on anti-scattering imaging than those near 500 MHz. Therefore, they allocate more attention to these frequency components. Besides, the distribution obtained through AAM is a more powerful generalized bandpass filter. Although the learning mechanisms of current deep learning technologies still lack interpretability, the counterintuitive results obtained by the network may provide research insights for physical optics researchers to establish more comprehensive physical models of water bodies or guide algorithm researchers to design more advanced manual filters.

#### E. DBC-Attention is more suitable for underwater optical 3D imaging than Self-Attention

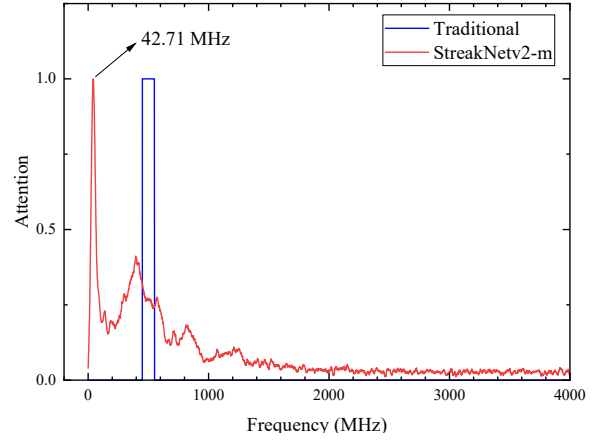
To validate the superiority of DBC-Attention over Self-Attention in underwater imaging tasks, we designed and conducted ablation experiments. StreakNet2, compared to StreakNet, replaces the backbone network from Self-Attention to DBC-Attention, while keeping the other parameters unchanged. Through the experimental results (Fig. 7 and Table III), we found:

- **Regarding anti-scattering performance:** Except for the m-model, the  $F_1$  scores of StreakNet2 on s, l, and x models is higher than StreakNet, indicating that the average anti-scattering performance of DBC-Attention is superior to Self-Attention.
- **Regarding anti-overfitting performance:** The number of network parameters of s, m, l, x models increase sequentially. The  $F_1$  scores of StreakNet and StreakNet2 increases from s to m and decreases thereafter, indicating varying degrees of overfitting in both architectures after

Fig. 12. Curve of AIT (ms) with the changing number  $N$  of streak-tube images.

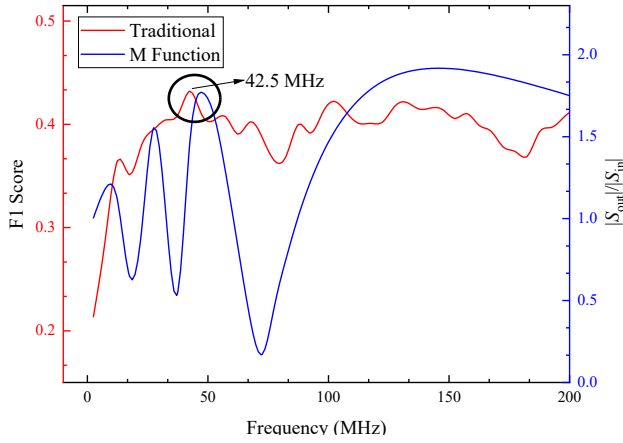


(a) Attention distribution with frequency after AAM analysis for StreakNet-m.

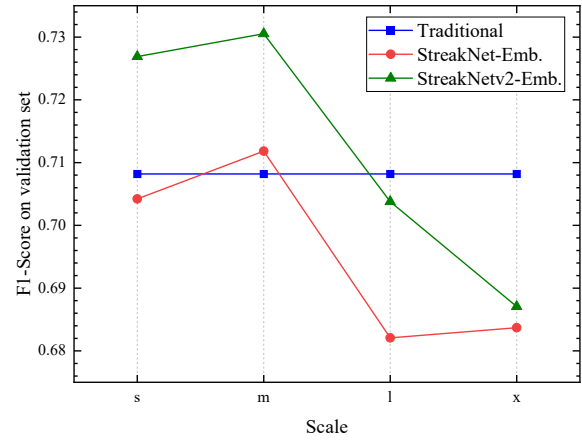


(b) Attention distribution with frequency after AAM analysis for StreakNetv2-m.

Fig. 13. Results of attention distribution with frequency after AAM analysis.

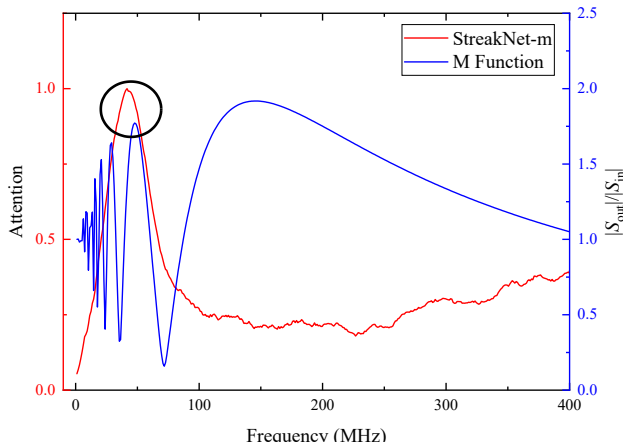


(a) The  $F_1$  scores on the validation set for imaging results using traditional bandpass filters in different frequency ranges (red curve, left), and the curve of  $\mathcal{M}$  Function (blue curve, right).

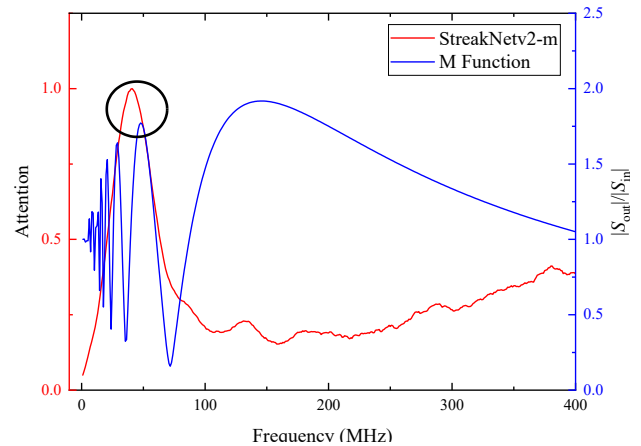


(b) The  $F_1$  scores on the validation set for imaging using traditional bandpass filtering methods and imaging using the generalized bandpass filter obtained directly from AAM.

Fig. 14. Results of bandpass range enumeration experiment and network ablation experiment.



(a) Attention distribution of StreakNet-m and the curve of  $\mathcal{M}$  Function.



(b) Attention distribution of StreakNetv2-m and the curve of  $\mathcal{M}$  Function.

Fig. 15. The curve of Attention distribution of StreakNets and the curve of  $\mathcal{M}$  Function.



the m-model. Although StreakNet’s performance is significantly higher than StreakNetv2 on the m-model, it significantly decreases on the x-model. Overall, StreakNet shows large fluctuations in anti-scattering performance from s to x, while StreakNetv2 remains relatively stable, indicating that DBC-Attention has stronger anti-overfitting performance than Self-Attention in underwater imaging tasks.

We simultaneously conducted ablation experiments with traditional imaging methods. We performed Attention Analysis on the FD Embedding Layer of both StreakNet and StreakNetv2. The results were used as equivalent filters, replacing the traditional 450 MHz - 550 MHz bandpass filter for imaging, and the imaging outcomes are shown in Fig. 8e-l and Fig. 9e-l. The results on the validation set are presented in Fig. 14b and Table V.

TABLE V  
F<sub>1</sub> SCORES (%) FOR TRADITIONAL IMAGING METHODS AND AAM EQUIVALENT FILTERING IMAGING METHODS ON THE VALIDATION SET.

Model	Traditional (baseline)	StreakNet-Emb.	StreakNetv2-Emb.		
s	70.82	70.42	-0.39	72.69	+1.87
m	70.82	71.18	+0.36	73.05	<b>+2.24</b>
l	70.82	68.21	-2.61	70.38	-0.44
x	70.82	68.37	-2.45	68.71	-2.11

From the experimental results, it is evident that the overall performance of StreakNetv2-Emb is significantly better than StreakNet-Emb. This further demonstrates that the features learned by DBC-Attention exhibit stronger anti-scattering capabilities compared to Self-Attention.

## V. CONCLUSION

This paper tackles two significant challenges impeding conventional underwater imaging algorithms: limited anti-scattering capabilities and the inability to achieve real-time processing. We incorporated Self-Attention mechanism networks into the signal processing stage to enhance the scatter resistance capability of the UCLR. Primarily, we introduce StreakNet-Arch, a groundbreaking end-to-end binary classification architecture, to overcome the real-time imaging hurdle. Additionally, DBC-Attention, a novel variant of the Self-Attention mechanism specifically optimized for underwater environments, is proposed. Experimental results conclusively demonstrate DBC-Attention’s superiority, achieving significantly better performance compared to the standard Self-Attention approach. Furthermore, we have released the first-ever public dataset containing 2,695,168 real-world underwater 3D point cloud data of streak-tube camera images. This work paves the way for future research on optimizing filtering methods in underwater imaging algorithms.

## REFERENCES

- [1] Z. Zhao, Y. Liu, X. Sun, J. Liu, X. Yang, and C. Zhou, “Composited fishnet: Fish detection and species recognition from low-quality underwater videos,” *IEEE Transactions on Image Processing*, vol. 30, pp. 4719–4734, 2021.
- [2] H.-M. Hu, Q. Guo, J. Zheng, H. Wang, and B. Li, “Single image defogging based on illumination decomposition for visual maritime surveillance,” *IEEE Transactions on Image Processing*, vol. 28, no. 6, pp. 2882–2897, 2019.
- [3] C. Lin, Y. Cheng, X. Wang, J. Yuan, and G. Wang, “Transformer-based dual-channel self-attention for uuv autonomous collision avoidance,” *IEEE Transactions on Intelligent Vehicles*, vol. 8, no. 3, pp. 2319–2331, 2023.
- [4] X. Wang, “Active fault tolerant control for unmanned underwater vehicle with actuator fault and guaranteed transient performance,” *IEEE Transactions on Intelligent Vehicles*, vol. 6, no. 3, pp. 470–479, 2021.
- [5] L. Peng, C. Zhu, and L. Bian, “U-shape transformer for underwater image enhancement,” *IEEE Transactions on Image Processing*, vol. 32, pp. 3066–3079, 2023.
- [6] R. Cong, W. Yang, W. Zhang, C. Li, C.-L. Guo, Q. Huang, and S. Kwong, “Pugan: Physical model-guided underwater image enhancement using gan with dual-discriminators,” *IEEE Transactions on Image Processing*, vol. 32, pp. 4472–4485, 2023.
- [7] Q. Qi, K. Li, H. Zheng, X. Gao, G. Hou, and K. Sun, “Sguie-net: Semantic attention guided underwater image enhancement with multi-scale perception,” *IEEE Transactions on Image Processing*, vol. 31, pp. 6816–6830, 2022.
- [8] Z. Wang, L. Shen, M. Xu, M. Yu, K. Wang, and Y. Lin, “Domain adaptation for underwater image enhancement,” *IEEE Transactions on Image Processing*, vol. 32, pp. 1442–1457, 2023.
- [9] Y. Zheng, W. Chen, R. Lin, T. Zhao, and P. Le Callet, “Uif: An objective quality assessment for underwater image enhancement,” *IEEE Transactions on Image Processing*, vol. 31, pp. 5456–5468, 2022.
- [10] P. Zhuang, J. Wu, F. Porikli, and C. Li, “Underwater image enhancement with hyper-laplacian reflectance priors,” *IEEE Transactions on Image Processing*, vol. 31, pp. 5442–5455, 2022.
- [11] R. Liu, Z. Jiang, S. Yang, and X. Fan, “Twin adversarial contrastive learning for underwater image enhancement and beyond,” *IEEE Transactions on Image Processing*, vol. 31, pp. 4922–4936, 2022.
- [12] C. Li, S. Anwar, J. Hou, R. Cong, C. Guo, and W. Ren, “Underwater image enhancement via medium transmission-guided multi-color space embedding,” *IEEE Transactions on Image Processing*, vol. 30, pp. 4985–5000, 2021.
- [13] J. Zhou, Q. Gai, D. Zhang, K.-M. Lam, W. Zhang, and X. Fu, “Iacc: Cross-illumination awareness and color correction for underwater images under mixed natural and artificial lighting,” *IEEE Transactions on Geoscience and Remote Sensing*, vol. 62, pp. 1–15, 2024.

- [14] S. Yan, X. Chen, Z. Wu, M. Tan, and J. Yu, "Hybrur: A hybrid physical-neural solution for unsupervised underwater image restoration," *IEEE Transactions on Image Processing*, vol. 32, pp. 5004–5016, 2023.
- [15] Y.-T. Peng and P. C. Cosman, "Underwater image restoration based on image blurriness and light absorption," *IEEE Transactions on Image Processing*, vol. 26, no. 4, pp. 1579–1594, 2017.
- [16] Z. Liang, X. Ding, Y. Wang, X. Yan, and X. Fu, "Gudcp: Generalization of underwater dark channel prior for underwater image restoration," *IEEE Transactions on Circuits and Systems for Video Technology*, vol. 32, no. 7, pp. 4879–4884, 2022.
- [17] L. Mullen, P. Herczfeld, and V. Contarino, "Modulated pulse lidar system for shallow underwater target detection," in *Proceedings of OCEANS'94*, vol. 1. IEEE, 1994, pp. I-835.
- [18] L. Mullen, A. Vieira, P. Herczfeld, and V. Contarino, "Microwave-modulated transmitter design for hybrid lidar-radar," in *Proceedings of 1995 IEEE MTT-S International Microwave Symposium*. IEEE, 1995, pp. 1495–1498.
- [19] L. J. Mullen and V. M. Contarino, "Hybrid lidar-radar: seeing through the scatter," *IEEE Microwave magazine*, vol. 1, no. 3, pp. 42–48, 2000.
- [20] S. O'Connor, R. Lee, L. Mullen, and B. Cochenour, "Waveform design considerations for modulated pulse lidar," in *Ocean Sensing and Monitoring VI*, W. W. Hou and R. A. Arnone, Eds., vol. 9111, International Society for Optics and Photonics. SPIE, 2014, p. 91110P.
- [21] J. Cariou and J. Lotrian, "Transmission characteristics of a pulsed laser beam in natural sea-water: determination of the attenuation coefficients in the 415-660 nm spectral range," *Journal of Physics D: Applied Physics*, vol. 15, no. 10, p. 1873, 1982.
- [22] F. Pellen, X. Intes, P. Olivard, Y. Guern, J. Cariou, and J. Lotrian, "Determination of sea-water cut-off frequency by backscattering transfer function measurement," *Journal of Physics D: Applied Physics*, vol. 33, no. 4, p. 349, 2000.
- [23] F. Pellen, P. Olivard, Y. Guern, J. Cariou, and J. Lotrian, "Radio frequency modulation on an optical carrier for target detection enhancement in sea-water," *Journal of Physics D: Applied Physics*, vol. 34, no. 7, pp. 1122–1130, Apr. 2001.
- [24] K. Takahashi, H. Takayama, S. Kobayashi, M. Takeda, Y. Nagata, K. Karashima, K. Takaki, and T. Namihira, "Observation of the development of pulsed discharge inside a bubble under water using iccd cameras," *Vacuum*, vol. 182, p. 109690, 2020.
- [25] G. Li, Q. Zhou, G. Xu, X. Wang, W. Han, J. Wang, G. Zhang, Y. Zhang, S. Song, S. Gu *et al.*, "Lidar-radar for underwater target detection using a modulated sub-nanosecond q-switched laser," *Optics & Laser Technology*, vol. 142, p. 107234, 2021.
- [26] L. Griffiths, "An adaptive lattice structure for noise-cancelling applications," in *ICASSP '78. IEEE International Conference on Acoustics, Speech, and Signal Processing*, vol. 3, 1978, pp. 87–90.
- [27] J. Makhoul, "A class of all-zero lattice digital filters: Properties and applications," *IEEE Transactions on Acoustics, Speech, and Signal Processing*, vol. 26, no. 4, pp. 304–314, 1978.
- [28] S. Boll, "Adaptive noise cancelling in speech using the short-time transform," in *ICASSP '80. IEEE International Conference on Acoustics, Speech, and Signal Processing*, vol. 5, 1980, pp. 692–695.
- [29] B. Widrow and J. McCool, "A comparison of adaptive algorithms based on the methods of steepest descent and random search," *IEEE Transactions on Antennas and Propagation*, vol. 24, no. 5, pp. 615–637, 1976.
- [30] E. Ferrara, "Fast implementations of lms adaptive filters," *IEEE Transactions on Acoustics, Speech, and Signal Processing*, vol. 28, no. 4, pp. 474–475, 1980.
- [31] D. Mansour and A. Gray, "Unconstrained frequency-domain adaptive filter," *IEEE Transactions on Acoustics, Speech, and Signal Processing*, vol. 30, no. 5, pp. 726–734, 1982.
- [32] D. W. Illig, K. X. Kocan, and L. J. Mullen, "Machine learning applied to the underwater radar-encoded laser system," in *Global Oceans 2020: Singapore-US Gulf Coast*. IEEE, 2020, pp. 1–6.
- [33] N. Otsu *et al.*, "A threshold selection method from gray-level histograms," *Automatica*, vol. 11, no. 285-296, pp. 23–27, 1975.
- [34] S. Chakraverty, D. M. Sahoo, and N. R. Mahato, *McCulloch-Pitts Neural Network Model*. Singapore: Springer Singapore, 2019, pp. 167–173.
- [35] A. Vaswani, N. Shazeer, N. Parmar, J. Uszkoreit, L. Jones, A. N. Gomez, Ł. Kaiser, and I. Polosukhin, "Attention is all you need," *Advances in neural information processing systems*, vol. 30, 2017.
- [36] J. Hu, L. Shen, and G. Sun, "Squeeze-and-excitation networks," in *Proceedings of the IEEE conference on computer vision and pattern recognition*, 2018, pp. 7132–7141.
- [37] X. Wang, R. Girshick, A. Gupta, and K. He, "Non-local neural networks," in *Proceedings of the IEEE conference on computer vision and pattern recognition*, 2018, pp. 7794–7803.
- [38] M.-H. Guo, J.-X. Cai, Z.-N. Liu, T.-J. Mu, R. R. Martin, and S.-M. Hu, "Pct: Point cloud transformer," *Computational Visual Media*, vol. 7, pp. 187–199, 2021.
- [39] A. Dosovitskiy, L. Beyer, A. Kolesnikov, D. Weissenborn, X. Zhai, T. Unterthiner, M. Dehghani, M. Minderer, G. Heigold, S. Gelly, J. Uszkoreit, and N. Houlsby, "An image is worth 16x16 words: Transformers for image recognition at scale," in *Proceedings of International Conference on Learning Representations*, 2021.
- [40] L. Yuan, Y. Chen, T. Wang, W. Yu, Y. Shi, Z.-H. Jiang, F. E. Tay, J. Feng, and S. Yan, "Tokens-to-token vit: Training vision transformers from scratch on imagenet," in *Proceedings of the IEEE/CVF international conference on computer vision*, 2021, pp. 558–567.
- [41] J. Devlin, M.-W. Chang, K. Lee, and K. Toutanova, "Bert: Pre-training of deep bidirectional transformers for

language understanding,” in *North American Chapter of the Association for Computational Linguistics*, 2019.

- [42] Z. Yang, Z. Dai, Y. Yang, J. Carbonell, R. R. Salakhutdinov, and Q. V. Le, “Xlnet: Generalized autoregressive pretraining for language understanding,” *Advances in neural information processing systems*, vol. 32, 2019.
- [43] V. Mnih, N. Heess, A. Graves *et al.*, “Recurrent models of visual attention,” *Advances in neural information processing systems*, vol. 27, 2014.
- [44] K. Xu, J. Ba, R. Kiros, K. Cho, A. Courville, R. Salakhutdinov, R. Zemel, and Y. Bengio, “Show, attend and tell: Neural image caption generation with visual attention,” in *International conference on machine learning*. PMLR, 2015, pp. 2048–2057.
- [45] K. Gregor, I. Danihelka, A. Graves, D. Rezende, and D. Wierstra, “Draw: A recurrent neural network for image generation,” in *International conference on machine learning*. PMLR, 2015, pp. 1462–1471.
- [46] J. Zhuang, B. Gong, L. Yuan, Y. Cui, H. Adam, N. Dvornik, S. Tatikonda, J. Duncan, and T. Liu, “Surrogate gap minimization improves sharpness-aware training,” 2022.
- [47] X. Zhai, X. Wang, B. Mustafa, A. Steiner, D. Keysers, A. Kolesnikov, and L. Beyer, “Lit: Zero-shot transfer with locked-image text tuning,” 2022.
- [48] M. Ummar, F. A. Dharejo, B. Alawode, T. Mahbub, M. J. Piran, and S. Javed, “Window-based transformer generative adversarial network for autonomous underwater image enhancement,” *Engineering Applications of Artificial Intelligence*, vol. 126, p. 107069, 2023.
- [49] A. Pramanick, S. Sarma, and A. Sur, “X-caunet: Cross-color channel attention with underwater image-enhancing transformer,” in *ICASSP 2024 - 2024 IEEE International Conference on Acoustics, Speech and Signal Processing (ICASSP)*, 2024, pp. 3550–3554.
- [50] S. Imambi, K. B. Prakash, and G. Kanagachidambaresan, “Pytorch,” *Programming with TensorFlow: Solution for Edge Computing Applications*, pp. 87–104, 2021.
- [51] J. L. Ba, J. R. Kiros, and G. E. Hinton, “Layer normalization,” 2016.
- [52] P. Ramachandran, B. Zoph, and Q. V. Le, “Searching for activation functions,” *CoRR*, vol. abs/1710.05941, 2017.
- [53] P. Perez, W. D. Jemison, L. Mullen, and A. Laux, “Techniques to enhance the performance of hybrid lidar-radar ranging systems,” in *2012 Oceans*. Hampton Roads, VA: IEEE, Oct. 2012, pp. 1–6.



**Xuelong Li** is the Chief Technology Officer (CTO) of China Telecom since 2023. Before that, he was a full professor at The Northwestern Polytechnical University (2018-2023), a full professor at The Chinese Academy of Sciences (2009-2018), a Lecturer/Senior Lecturer/Reader at The University of London (2004-2009), a Lecturer at The University of Ulster (2003-2004), and he previously took positions at The Chinese University of Hong Kong, The Hong Kong University, The Microsoft Research, and The Huawei Technologies Co., Ltd.



**Hongjun An** received the bachelor’s degree in information Science and Technology College from Dalian Maritime University, Dalian, China, in 2024. He is currently pursuing the Ph.D. degree with the School of Artificial Intelligence, Optics and ElectroNics (iOPEN) from Northwestern Polytechnical University, Xi’an, China. His research interests include water-related optics, unmanned underwater vehicles (UUVs), large models (LMs) and embodied intelligent robots.



**Guangying Li** is the research assistant of Xi’an Institute of Optics and Precision Mechanics, Chinese Academy of Sciences since 2022. He received his PhD degrees from University of Chinese Academy of Sciences. He is engaged in ultrafast solid-state laser technology, as well as underwater laser communication and detection technology research.



**Xing Wang** is currently a Professor at Xi’an Institute of Optics and Precision Mechanics, Chinese Academy of Sciences. His research interests include ultrafast and ultra-sensitive photoelectric detection devices, ultrafast diagnostic cameras and 3D imaging Lidar. He has coauthored more than 50 papers. He serves as young editors of *Ultrafast Sciences* and *Acta Photonica Sinica*.



**Guanghua Cheng** is currently a Professor in School of Artificial Intelligence, Optics and Electronics (iOPEN), Northwestern Polytechnical University, Xi’an, China. Also, he is a visiting Professor in Laboratoire Hubert Curien, UMR 5516 CNRS, Université Jean Monnet, Saint Etienne, France. His research interests include Interaction between ultrafast laser and mater, ultrafast laser machining, high power solid laser technique, and nonlinear optics.



**Zhe Sun** is currently an Associate Professor of Northwestern Polytechnical University since 2022. Before that, he was a postdoc at Friedrich Schiller University Jena (2020-2022) and Helmholtz Institute Jena, GSI Helmholtzzentrum für Schwerionenforschung GmbH (2018-2020). Previously, he contributed as a research assistant at the Xi’an Institute of Optics and Precision Mechanics, Chinese Academy of Sciences (2014-2018). He received his PhD degrees from the Beijing University of Technology. His research interests include water-related optics, computational imaging, laser imaging.